REPORT DOCUMENTATION PAGE

Form Approved OMB No. 0704-0188

1. REPORT DATE *(DD-MM-YYYY)*	2. REPORT TYPE	3. DATES COVERED *(From – To)*
10-05-2006	Final Report	1 May 2005 - 31-May-06

4. TITLE AND SUBTITLE

Transverse Laser Patterns: Quantitative Validation Of The Order Parameter Equation

5a. CONTRACT NUMBER
FA8655-05-1-3040

5b. GRANT NUMBER

5c. PROGRAM ELEMENT NUMBER

6. AUTHOR(S)

Dr. Carlos Martel

5d. PROJECT NUMBER

5d. TASK NUMBER

5e. WORK UNIT NUMBER

7. PERFORMING ORGANIZATION NAME(S) AND ADDRESS(ES)

Universidad Politecnica of Madrid
Avenida Ramiro de Maeztu,7
Ciudad Universitaria
Madrid 28040
Spain

8. PERFORMING ORGANIZATION REPORT NUMBER

N/A

9. SPONSORING/MONITORING AGENCY NAME(S) AND ADDRESS(ES)

EOARD
PSC 821 BOX 14
FPO 09421-0014

10. SPONSOR/MONITOR'S ACRONYM(S)

11. SPONSOR/MONITOR'S REPORT NUMBER(S)
Grant 05-3040

12. DISTRIBUTION/AVAILABILITY STATEMENT

Approved for public release; distribution is unlimited.

13. SUPPLEMENTARY NOTES

14. ABSTRACT

This report results from a contract tasking Universidad Politecnica of Madrid as follows: The proposed research work will be carried out in 3 steps:

(I) Derivation of the order parameter equation from the MB equations using multiple scales techniques.

(II) Numerical codes for the integration of the MB and CSH equations.

IIa) Development of a numerical code for the efficient computation of the solutions of the time-dependent MB equations in a 2D extended spatial domain.

IIb) Development of a numerical code for the integration of the time-dependent 2D complex Swift-Hohenberg equation.

(III) Numerical simulation of the MB equations for different (large) spatial domain sizes and different (small) subcriticalities. Quantitative comparison with the solutions obtained from the CSH equation.

FACILITIES/EQUIPMENT

Two INTEL PC's running linux with computational software (C,Fortran, Matlab and Maple) installed and access to several laser printers constitute the existing equipment that will be used. One newer and faster Intel PC (with dual CPU) will be purchased and dedicated to perform the intensive numerical computations required to complete this research.

The research project will last 1 year. One report will be delivered at the end of the project and a progress report could be delivered after the first 6 months.

15. SUBJECT TERMS

EOARD, Laser modeling, Laser resonators, Laser physics

16. SECURITY CLASSIFICATION OF:			17. LIMITATION OF ABSTRACT	18, NUMBER OF PAGES	19a. NAME OF RESPONSIBLE PERSON
a. REPORT	b. ABSTRACT	c. THIS PAGE			DONALD J SMITH
UNCLAS	UNCLAS	UNCLAS	UL	43	19b. TELEPHONE NUMBER *(Include area code)* +44 (0)20 7514 4953

Transverse laser patterns: quantitative validation of the order parameter equation description

April 28, 2006

Final report to the European Office of Aerospace Research and Development
Research grant: FA8655-05-1-3040

Carlos Martel (martel@fmetsia.upm.es)
Alejandro Fernández
Depto. Fundamentos Matemáticos
E.T.S.I. Aeronáuticos
Universidad Politécnica de Madrid
28040 Madrid, SPAIN

Contents

1 Introduction

The nonlinear transverse dynamics of single longitudinal mode lasers in cavities is described by the Maxwell-Bloch (MB) equations that account for the interaction of the electromagnetic field with the active media inside the cavity. Several different order parameter equations have been derived from the MB equations and are currently used to gain some understanding of transverse pattern forming instabilities in lasers (see, e.g., the recent reviews [1] and [2]). The study of these order parameter equations (OP) is interesting not only for the analysis of the transverse nonlinear dynamics of lasers, but also from the more general point of view of pattern formation in general spatially extended systems, because the same OP equations can be used to describe other physical systems that exhibit the same basic destabilization mechanism [3].

The derivation of the OP equations from the MB equations is based on the slow envelope assumption, i.e., on the assumption that the amplitudes of the physical fields are small and depend slowly on time and on the transversal spatial scales. But the OP equations are commonly applied without observing the slow envelope requirement, and it is not infrequent to find in the literature solutions of the OP equations that do not exhibit only long scales. This is normally justified by saying that the OP equations retain the essential dynamics of the system and thus its range of application can be somehow extended and they still provide "qualitative" information about the patterns and instabilities that take place in the original physical system (see [1, 2] and the references therein).

The main goal of this research work is to go beyond the qualitative description and quantitatively validate the OP equations to show how accurate and precise are the predictions they provide about the dynamic states and transitions that take place in the transverse laser profiles.

To this end, we will first apply multiple scales techniques to the MB equations to derive the corresponding OP equation and its coefficients in terms of the physical parameters of the problem. For the laser parameter values that we will consider, namely class C with small detuning, the resulting OP equation is a complex Swift-Hohenberg (CSH) equation [4, 5]. In this case, due to the small value of the detuning, the diffusion of the system acts on a much slower time scale than the dispersion

and, if the slow envelope assumption is consistently applied, this scale disparity is inherited by the CSH equation that necessarily includes terms of different asymptotic order and, in in some particular regimes, it even allow us to further simplify the resulting CSH to a complex Ginzburg-Landau (CGL) equation. This unavoidable asymptotic nonuniformity of the resulting CSH equation is not properly taken into account in the usual analyses in the literature, where, invoking the argument of the qualitative only scope of the OP description, a CSH equation with all terms of the same order is normally used to analyze this laser instability. In order to clarify this point, we carry out in this research effort numerical integrations of both, the MB equations in an extended spatial domain and the CSH equation, that allow us to confirm that the quantitatively correct weakly nonlinear description of the MB system is given by the above mentioned, asymptotically nonuniform CSH equation (and, in some cases, by the simpler CGL equation).

This report is organized as follows. In the next Section we introduce our physical model for the laser transverse dynamics, the MB equations, and study the basic linear stability characteristics of the non-lasing state in a class C laser with small detuning. The derivation of the corresponding CSH equation that describe the near onset dynamics of the system is carried out in Section 3 and the simplest patterns (travelling waves and spiral waves) displayed by the system and their stability properties are analyzed in Section 4. Finally, Section 5 contains some numerical simulations of the CSH equation performed in order to check the presence of two asymptotically different scales, and the description and results of the procedure implemented in order to quantitative compare the solutions the MB and CSH, together with a brief explanation of the numerical methods used to integrate both, the MB and CSH equations.

2 Maxwell-Bloch model

The dynamics of a two-level laser in the 2D plane section transverse to the main propagation direction of the electromagnetic wave is governed by the well-known Maxwell-Bloch (MB) equations [6] that, in the simple case of a single longitudinal mode, can be written as

$$\frac{\partial E}{\partial t} = ia\nabla^2 E - \sigma E + \sigma P, \tag{1}$$

$$\frac{\partial P}{\partial t} = -(1 + i\Omega)P + (r - N)E, \tag{2}$$

$$\frac{\partial N}{\partial t} = -bN + \frac{1}{2}(\overline{E}P + E\overline{P}). \tag{3}$$

We are using here the same nondimensional formulation as in [7], where $E(x, y, t)$ and $P(x, y, t)$ represent the complex electric and polarization fields, $N(x, y, t)$ is the real valued field of the population inversion, $a > 0$ measures the strength of the diffraction, $\sigma > 0$ and Ω account for the cavity losses and the cavity detuning, r is the pumping parameter, $b > 0$ is the decay rate of the population inversion, $\nabla^2 = \partial^2/\partial x^2 + \partial^2/\partial y^2$ is the 2D laplacian operator and the bar stands for the complex conjugate. In the equations above the size of the fields have been scaled in order to remove the coefficients of the nonlinear terms and time is measured using the characteristic decay time of the polarization. Note also that the diffraction coefficient, a, can be set to 1 without loss of generality (as we will do hereafter) just by scaling the space variables $\mathbf{x} = (x, y)$ with the diffraction length $\sqrt{a}$.

Lasers are usually classified according to the relative value of the decay rate of the population difference $\gamma_\parallel$, the cavity decay rate κ, and the decay rate of the polarization $\gamma_\perp$: for a class A laser, $\gamma_\perp$, $\gamma_\parallel \gg \kappa$; for a class B laser, $\gamma_\perp \gg \kappa \gg \gamma_\parallel$; and all decay rates are comparable for a class C laser, $\kappa \sim \gamma_\perp \sim \gamma_\parallel$, see e.g. [8]. We will focus our attention on class C lasers that, in the nondimensional formulation of eqs. (1)-(3) where time has been scaled with $\gamma_\perp$ and $\sigma = \kappa/\gamma_\perp$ and $b = \gamma_\parallel/\gamma_\perp$, correspond to $\sigma \sim 1$ and $b \sim 1$.

The linear stability properties of the basic nonlasing state $(E, P, N) = (0, 0, 0)$

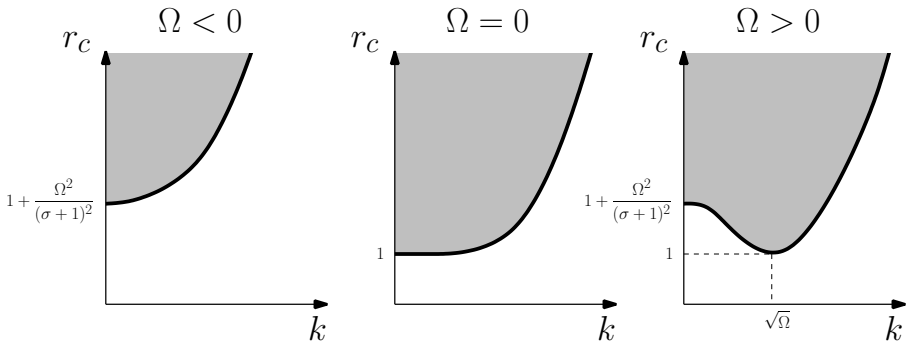

Figure 1: MB zero state neutral stability curves for $\Omega < 0$, $\Omega = 0$ and $\Omega > 0$ (shading indicates instability).

are readily calculated inserting the ansatz

$$\begin{bmatrix} E(x,y,t) \\ P(x,y,t) \\ N(x,y,t) \end{bmatrix} = \begin{bmatrix} E \\ P \\ N \end{bmatrix}_{\mathbf{k}} \mathrm{e}^{\mathrm{i}\mathbf{k}\cdot\mathbf{x}+\lambda t}$$

into the linearized version of the MB and solving the resulting eigenvalue problem,

$$\begin{bmatrix} \lambda+\sigma+\mathrm{i}k^2 & -\sigma & 0 \\ -r & \lambda+1+\mathrm{i}\Omega & 0 \\ 0 & 0 & \lambda+b \end{bmatrix} \begin{bmatrix} E \\ P \\ N \end{bmatrix}_{\mathbf{k}} = \begin{bmatrix} 0 \\ 0 \\ 0 \end{bmatrix},$$

which gives the following stability exponents, λ, as a function of the wavevector, $\mathbf{k} = (k_x, k_y)$,

$$\lambda = -b, \tag{4}$$

$$\lambda = -\frac{\sigma+1+\mathrm{i}(k^2+\Omega)}{2} \pm \frac{\sqrt{((\sigma-1)+\mathrm{i}(k^2-\Omega))^2+4r\sigma}}{2}, \tag{5}$$

with $k^2 = |\mathbf{k}|^2$. After some tedious algebra, one can see that the zero solution is stable if the pump, r, is below the critical value

$$r_c = 1 + \frac{(k^2-\Omega)^2}{(\sigma+1)^2},$$

and unstable otherwise [4, 5].

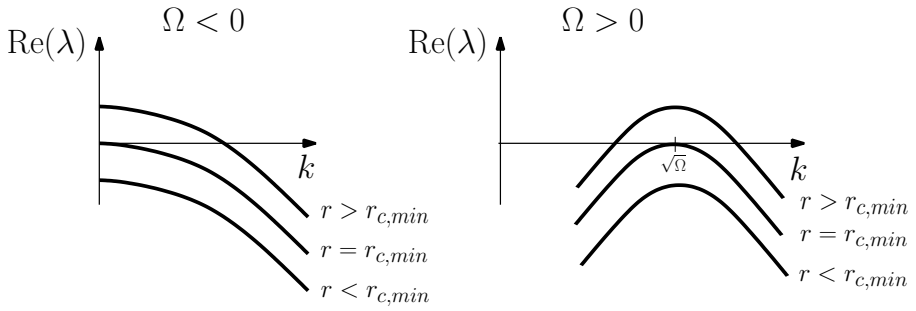

Figure 2: Growth rate of the MB almost neutral modes near onset for $\Omega < 0$ and $\Omega > 0$.

Figure 1 shows the resulting neutral stability curves, i.e., the critical value of the pump r_c, against the wavenumber k for different values of Ω. When $\Omega < 0$, the most unstable mode is $k = 0$, while when $\Omega > 0$ the most unstable modes lie along a circumference (in the plane k_x-k_y) of radius $k = \sqrt{\Omega}$. These are the modes that first become unstable when the pump is increased over the lasing threshold $r_{c,min}$, which is given by $r_{c,min} = 1 + \frac{\Omega^2}{(\sigma+1)^2}$ for $\Omega < 0$ and $r_{c,min} = 1$ for $\Omega > 0$.

Let us consider now that the system is close to threshold: $r = r_{c,min} + \epsilon$, with $|\varepsilon| \ll 1$. The order of magnitude of the unstable wavenumbers can be determined from Fig. 2. If $\Omega < 0$, then $k \sim \sqrt{|\epsilon|}$ and, using scale separation and applying solvability conditions, a well known complex Ginzburg-Landau (CGL) equation is straightforwardly obtained [7] for the weakly nonlinear description of the system dynamics. If, on the other hand, $\Omega > 0$, then the circumference of neutral modes in the plane k_x-k_y becomes a thin annulus of unstable modes of width $\Delta k \sim \sqrt{|\epsilon|}$ (see Fig. 2). In this case a a pair of counter-propagating coupled CGL equations can be obtained for 1D and quasi-1D configurations [7, 9, 10], but the OP equation that completely describes this incipient destabilization in 2D is not currently known, and it still constitutes one of the open problems in pattern formation [3].

This report covers the transitional case of small detuning $|\Omega| \ll 1$ in a class C laser, which is described by a complex Swift-Hohenberg (CSH) equation [4, 5]. The CSH can be also obtained for class A lasers, and even for class B lasers (e.g., CO_2 and semiconductor lasers), but starting from a more specific set of equations [11, 12]. A detailed derivation of the CSH from the MB equations, where special emphasis is placed on the asymptotic order of its different terms, is presented in the next section.

3 Order parameter equation for small detuning

In this section we derive the slow envelope equation that describes the transverse laser patterns displayed by the MB equations (1)-(3) right after onset, in the small detuning case.

Near the destabilization threshold, the weakly nonlinear dynamics of the system is dominated by its linear part and the order of magnitude of the slow scales that the system exhibits can be obtained from the study of the behavior of the branch of eigenvalues responsible for the stability change. The small nonlinearities of the problem do not play any role in the slow scale selection; they just define the characteristic size of the resulting pattern through the saturation of the instability growth, and they will be taken into account later on.

For small detuning, the modes of the system that first become unstable are those corresponding to small wavevectors, and their linear stability characteristics are given by expression (5) with the + sign, which can be expanded as

$$\mathrm{Re}(\lambda) = \frac{\sigma}{\sigma+1}(r-1) - \frac{\sigma}{(\sigma+1)^3}(k^2-\Omega)^2 + \cdots , \tag{6}$$

$$\mathrm{Im}(\lambda) = -\frac{k^2+\sigma\Omega}{\sigma+1} + \cdots , \tag{7}$$

in the limit of small detuning, small displacement from threshold and small wavevector, i.e.,

$$|\Omega| \ll 1, \quad |r-1| \ll 1 \quad \text{and} \quad k \ll 1. \tag{8}$$

From the expression of the growth rate (6) we can see that the characteristic slow time is given by $\tau \sim 1/|r-1| \gg 1$ and that the range of almost neutral modes goes up to $k \sim |r-1|^{1/4}$ (see Fig. 3). The growth rate of the modes with $k \gg |r-1|^{1/4}$ is much larger and negative and therefore they are quickly damped out in the slow time scale. Note that in the scaling arguments above we are implicitly assuming that $|\Omega|$ is, at most, of the order of $|r-1|^{1/2}$. We are not considering the case $|\Omega| \gg |r-1|^{1/2}$ and $\Omega > 0$ ($\Omega < 0$ is stable and far from threshold), in which a narrow band of almost neutral modes of size $\Delta k \sim |r-1|^{1/2}/\sqrt{|\Omega|}$ develops around the critical wavevector circumference of radius $k_c \sim \sqrt{|\Omega|} \gg \Delta k$, because it corresponds to a completely different destabilization type, namely to that represented in Fig. 2 for $\Omega > 0$.

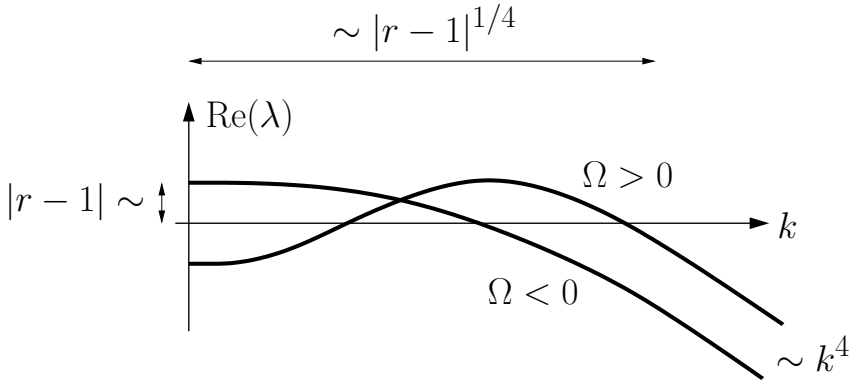

Figure 3: Sketch of the growth rate of the most unstable MB modes right after onset, for $|\Omega| \ll 1$, $|r-1| \ll 1$ and $k \ll 1$.

In other words, the behavior of the growth rate ensures that, for large times, the system can only exhibit spatial scales that are of the order $1/|r-1|^{1/4} \gg 1$ or larger, but no smaller ones, because those are damped out by the dominant linear effects.

On the other hand, the associated mode frequencies given by eq. (7) are always large as compared with the damping terms of the growth rate. This indicates that the effect of dispersion on the neutral modes of the system is faster and much stronger than that of diffusion. The envelope equation that describes the slow dynamics of the system has to take into account these two effects simultaneously and therefore it is necessarily going to contain terms of different asymptotic orders, which can never be rescaled to be of the same order. This is not the case in the transition represented in Fig. 2 for $\Omega < 0$, where dispersion and diffusion are both of the same order $\sim k^2$ and the weakly nonlinear dynamics of the system is described by an asymptotically uniform complex Ginzburg-Landau equation [7].

The need to retain terms of different orders made the derivation of the envelope equation presented in [4, 5] quite involved. They first assumed a particular scaling for the fields and the slow spatial and temporal variables, then they proceeded to derive the envelope equation and its next order correction, and, finally, they collapsed back the two term expansion into the original (unscaled) variables in order to obtain a single envelope equation.

The derivation of the envelope equation that we present below is, we believe, much more simple because we do not assume a priori any scaling relation between

the variables, we just look for small amplitude solutions that depend slowly on space and time (similar scaling free derivations can be found in [13] and [14] in the context of convection and water waves).

More precisely, the neutral mode at threshold, $r = 1$ and $\Omega = 0$, corresponds to $\lambda = 0$ and $k = 0$, with associated eigenvector

$$V_0 = \begin{bmatrix} 1 \\ 1 \\ 0 \end{bmatrix},$$

and suggests an expansion for the solution of the MB equations (1)-(3) of the form

$$\begin{bmatrix} E(x,y,t) \\ P(x,y,t) \\ N(x,y,t) \end{bmatrix} = V_0\psi \ + V_1\nabla^2\psi + \cdots, \tag{9}$$

where the complex amplitude $\psi(x,y,t)$ has to verify a solvability condition that is also expanded as

$$\psi_t = \alpha_0\psi + \alpha_1\nabla^2\psi + \cdots, \tag{10}$$

and is precisely the envelope equation that we are looking for. The expansions above include all possible combinations of the powers of the small quantities

$$|\Omega| \ll 1, \quad |r-1| \ll 1 \quad \text{and} \quad |\psi| \ll 1, |\nabla^2\psi| \ll 1, |\nabla^4\psi| \ll 1, \ldots$$

that are treated as independent parameters, only constrained by the weakly nonlinear level of this approach, which requires essentially that

$$\cdots \ll |\nabla^4\psi| \ll |\nabla^2\psi| \ll |\psi| \ll 1 \quad \text{and} \quad \cdots \ll |\psi_t| \ll |\psi| \ll 1 \ldots,$$

i.e., small envelope amplitude and slow time and space dependence (we have also anticipated the fact that only even order spatial derivatives will be produced because of the particular structure of the MB equations).

When the above expansions (9) and (10) are inserted in the MB equations (1)-(3), a linear nonhomogeneous singular system is obtained at each order. And, as it is the standard procedure in multiple scale methods to ensure that no secular

terms are present [15, 16], the nonhomogeneous terms of these systems must satisfy a solvability condition that provides the contribution of this order to the envelope equation.

The linear terms of the envelope equation (10) can be easily anticipated because they correspond to the Taylor expansion of the critical eigenvalue branch $\lambda(k^2, r, \Omega)$ (eq. (5) with the + sign) at $(k^2, r, \Omega) = (0, 1, 0)$ (see, e.g., [3]),

$$\lambda_{(0,1,0)}\psi + \left.\frac{\partial\lambda}{\partial r}\right|_{(0,1,0)}(r-1)\psi + \left.\frac{\partial\lambda}{\partial\Omega}\right|_{(0,1,0)}\Omega\psi - \left.\frac{\partial\lambda}{\partial(k^2)}\right|_{(0,1,0)}\nabla^2\psi + \\ + \frac{1}{2}\left.\frac{\partial^2\lambda}{\partial(k^2)^2}\right|_{(0,1,0)}\nabla^4\psi - \left.\frac{\partial^2\lambda}{\partial\Omega\partial(k^2)}\right|_{(0,1,0)}\Omega\nabla^2\psi + \frac{1}{2}\left.\frac{\partial^2\lambda}{\partial\Omega^2}\right|_{(0,1,0)}\Omega^2\psi + \ldots,$$

and thus, according to expressions (6) and (7), are of the form

$$\frac{\sigma}{\sigma+1}((r-1) - \mathrm{i}\Omega)\psi + \mathrm{i}\frac{1}{(\sigma+1)}\nabla^2\psi - \frac{\sigma}{(\sigma+1)^3}(\Omega + \nabla^2)^2\psi + \cdots \qquad (11)$$

The computation of the nonlinear terms requires to take the expansions (9) and (10) to the MB equations, which should be first rewritten in the more convenient form

$$\begin{bmatrix} \sigma & -\sigma & 0 \\ -1 & 1 & 0 \\ 0 & 0 & b \end{bmatrix}\begin{bmatrix} E \\ P \\ N \end{bmatrix} = -\frac{\partial}{\partial t}\begin{bmatrix} E \\ P \\ N \end{bmatrix} + \begin{bmatrix} \mathrm{i}\nabla^2 E \\ (r-1)E - \mathrm{i}\Omega P \\ 0 \end{bmatrix} + \begin{bmatrix} 0 \\ -NE \\ \frac{1}{2}(\overline{E}P + E\overline{P}) \end{bmatrix}, \quad (12)$$

with the dominant terms grouped in the left hand side. The first order nonlinear contribution to the expansions (9) and (10) is given by

$$V|\psi|^2 \quad \text{and} \quad \alpha|\psi|^2,$$

where the vector V and the scalar α are obtained from

$$\begin{bmatrix} \sigma & -\sigma & 0 \\ -1 & 1 & 0 \\ 0 & 0 & b \end{bmatrix} V = -\alpha V_0 + \begin{bmatrix} 0 \\ 0 \\ 1 \end{bmatrix}.$$

This system can only be solved if the right hand side is orthogonal to the solution

of the adjoint problem

$$V_0^a = \begin{bmatrix} 1 \\ \sigma \\ 0 \end{bmatrix},$$

and this solvability condition yields

$$V = \begin{bmatrix} 0 \\ 0 \\ \frac{1}{b} \end{bmatrix} \quad \text{and} \quad \alpha = 0.$$

Thus there is no contribution of this term to the envelope equation, in other words, it is not a resonant term. At next order we have the terms

$$W\psi|\psi|^2 \quad \text{and} \quad \beta\psi|\psi|^2,$$

which must verify

$$\begin{bmatrix} \sigma & -\sigma & 0 \\ -1 & 1 & 0 \\ 0 & 0 & b \end{bmatrix} W = -\beta V_0 + \begin{bmatrix} 0 \\ -\frac{1}{b} \\ 0 \end{bmatrix},$$

and, again, we apply the solvability condition to obtain the following coefficient of the envelope equation

$$\beta = -\frac{\sigma}{b(1+\sigma)}.$$

Finally, after collecting the leading nonlinear contribution above and the linear terms in (11), the envelope equation reads

$$\psi_t = \frac{\sigma((r-1) - \mathrm{i}\Omega)}{\sigma+1}\psi + \frac{\mathrm{i}}{(\sigma+1)}\nabla^2\psi - \frac{\sigma}{(\sigma+1)^3}(\Omega + \nabla^2)^2\psi - \frac{\sigma}{b(\sigma+1)}\psi|\psi|^2 + \cdots, \quad (13)$$

which is the well known complex Swift-Hohenberg equation (CSH) (see [4, 5]). It is important to stress that this equation has to be solved in the limit

$$|\Omega| \ll 1 \quad \text{and} \quad |r-1| \ll 1, \quad (14)$$

and that its solutions must verify the slow envelope assumption

$$\cdots \ll |\nabla^4\psi| \ll |\nabla^2\psi| \ll |\psi| \ll 1. \quad (15)$$

And therefore, as it was expected from the study of the growth rate, the CSH above contains different order terms: the effect of dispersion is always much bigger than the dissipation of the double diffusive term.

We now introduce the small parameter $0 < \varepsilon \ll 1$ and the scaling of the variables

$$(r-1) - \frac{\Omega^2}{(\sigma+1)^2} = \frac{(\sigma+1)^2}{\sigma^2}\alpha\varepsilon^2, \quad \tilde{t} = \frac{(\sigma+1)}{\sigma}t\varepsilon^2,$$
$$(\tilde{x},\tilde{y}) = \frac{(\sigma+1)}{\sqrt{\sigma}}(x,y)\varepsilon, \quad \psi = \mathrm{e}^{-\mathrm{i}\frac{\sigma\Omega}{(\sigma+1)}t}\sqrt{b}\frac{(\sigma+1)}{\sigma}\phi\varepsilon \quad , \Omega = \frac{(\sigma+1)^2}{\sigma}\omega\varepsilon, \quad (16)$$

which brings eq. (13), after dropping tildes, to the more convenient form

$$\phi_t = \alpha\phi + \mathrm{i}\nabla^2\phi - \phi|\phi|^2 - 2\varepsilon\omega\nabla^2\phi - \varepsilon^2\nabla^4\phi, \quad (17)$$

where the rescaled pump, α, and detuning, ω, are now order one parameters. Note that α can be also absorbed by means of a trivial change of variables, but we prefer to keep it because later on, when we perform some numerical integrations of eq. (17), it will allow us to make the scaled size of the domain independent of ε.

In the scaled CSH eq. (17) the dominant, dispersion induced dynamics is of order one: the typical length scale exhibited by the dispersive patterns (that was $\sim 1/\sqrt{|r-1|} \gg 1$ in the original variables) is now $\delta_{\mathrm{disp}} \sim 1$. On the other hand, the small coefficient multiplying the double diffusive term indicates that the system is capable of displaying scales as small as $\delta_{\mathrm{diff}} \sim \sqrt{\varepsilon}$ ($\sim 1/\sqrt[4]{|r-1|} \gg 1$ in the original variables) before diffusion becomes overwhelming and everything is damped out, recall Fig. 3.

The most simple solutions of eq. (17) are those that only exhibit scales $\sim \delta_{\mathrm{disp}} \sim 1$ as $\varepsilon \to 0$. For those dispersive states, the spatial derivatives remain of order one and thus the two last terms in eq. (17) represent, in the limit $\varepsilon \to 0$, a small correction that can be neglected to give

$$\phi_t = \alpha\phi + \mathrm{i}\nabla^2\phi - \phi|\phi|^2. \quad (18)$$

This is a very interesting complex Ginzburg-Landau equation (CGL) [3, 17, 18]: purely dispersive but with a dissipation that comes from the nonlinear term only. This CGL appears in a straightforward way from the small detuning MB equations due to the dominant character of the dispersion but, so far, we have not seen it

analyzed in the literature. Instead, the equations that are currently used to describe the weakly nonlinear dynamics of the MB equations in the small detuning case are either (i) the unscaled CSH eq. (13), but integrated without observing conditions (14) and (15), see [7, 4, 5, 19], or (ii) a CSH eq. scaled similarly to eq. (17), see [20], but again studied for $\varepsilon \sim 1$, when $\varepsilon \ll 1$ is the only physically relevant regime from the point of view of the slow envelope description of the transverse laser pattern dynamics.

Besides lasers, the CSH equation has been used as a model for other non-linear optical systems such as optical parametric oscillator [21, 22] and photorefractive materials, where the equation qualitatively reproduces experimental results [23].

4 Patterns

This section is dedicated to the study of some basic solutions of the CGL eq. (18), namely: spatially uniform travelling waves and spirals. Note that all solutions of the CGL are approximate solutions (up to $\mathcal{O}(\varepsilon)$ corrections) of the CSH, and once a stable solution of the CGL is found, in order to be sure that it is a stable state of the CSH, one must also check its stability under perturbations containing small diffusive scales, whose dynamics is not contained in the CGL.

As a previous step, we study the stability properties of the nonlasing solution $\phi = 0$. The solutions of the linearized version of the CSH in a square periodic domain can be written in the form

$$\phi \sim \mathrm{e}^{\mathrm{i}\mathbf{k}\cdot\mathbf{x}+\lambda t},$$

where λ is given by

$$\lambda = \alpha - \mathrm{i}k^2 + 2\varepsilon\omega k^2 - \varepsilon^2 k^4,$$

with $k = |\mathbf{k}|$ and $0 < \varepsilon \ll 1$. Two different kinds of perturbations can be distinguished. Those with wave vector $k \sim 1$, i.e., those exhibiting only dispersive scales $\delta_{\text{disp}} \sim 1$, for which the dispersion relation above simplifies to

$$\lambda = \alpha - \mathrm{i}k^2 + \ldots, \tag{19}$$

and thus are stable for $\alpha < 0$ and become unstable for $\alpha > 0$. The evolution of these perturbations is well represented by the CGL, which could have been used to obtain their stability properties. The second kind of perturbations are those with very high wave vector $k \sim K/\sqrt{\varepsilon} \gg 1$ and $K \sim 1$, which have a typical wavelength of the order of the small diffusive scales $\delta_{\text{diff}} \sim \sqrt{\varepsilon} \ll 1$, and whose growth rate is given by

$$\mathrm{Re}(\lambda) = \alpha + 2\omega K^2 - K^4. \tag{20}$$

For negative detuning $\omega < 0$ these small scale perturbations become unstable for positive α, but for $\omega > 0$ the destabilization takes place for $\alpha > -\omega^2$ at a critical wavenumber $k = \sqrt{\omega}/\sqrt{\varepsilon} \gg 1$. The dynamics of these perturbations is not included in the CGL and its analysis requires to deal with the complete CSH.

The structure of the growth rate of these perturbations is sketched in Fig. 4 and,

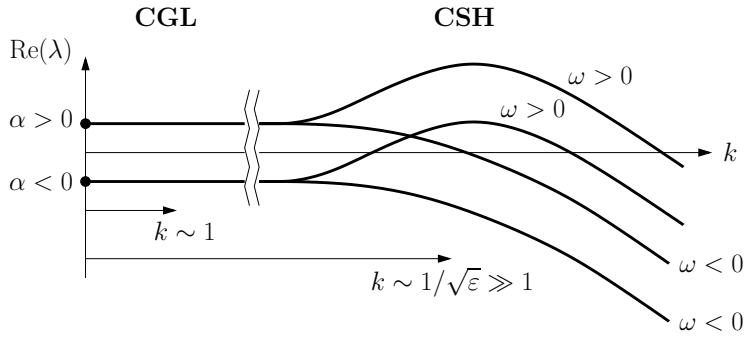

Figure 4: Growth rate of the perturbations of the zero solution of the CSH eq. (17) for $\omega > 0$ and $\omega < 0$, with the two wavenumber regions shown: $k \sim 1$ (dispersive perturbations) and $k \sim 1/\sqrt{\varepsilon} \gg 1$ (diffusive perturbations).

as it was expected, it is just a rescaled version of that obtained in the previous section for the MB, see Fig. 3. The resulting stability region of the nonlasing solution is the dark shaded area in the $\alpha - \omega$ plot in Fig. 5.

Inside the linear stability region depicted in Fig. 5, the zero solution is, in fact, globally stable, that is, all solutions of the CSH for all possible initial conditions decay to 0 as time increases. In order to see this, we multiply eq. (17) by $\bar{\phi}$, add the complex conjugate and integrate over the domain D to obtain

$$\frac{d}{dt}\int_D |\phi|^2 = 2\int_D |\phi|^2(\alpha - |\phi|^2) + \mathrm{i}\int_D (\bar{\phi}\nabla^2\phi - \phi\nabla^2\bar{\phi})$$
$$-2\varepsilon\omega\int_D (\bar{\phi}\nabla^2\phi + \phi\nabla^2\bar{\phi}) + \varepsilon^2\int_D (\bar{\phi}\nabla^4\phi + \phi\nabla^4\bar{\phi}).$$

If we now take into account that

$$\bar{\phi}\nabla^2\phi = \nabla\cdot(\bar{\phi}\nabla\phi) - |\nabla\phi|^2,$$

and apply Green's formula, the second integral above can be expressed as

$$\int_D \nabla\cdot(\bar{\phi}\nabla\phi - \phi\nabla\bar{\phi}) = \int_{\delta D} (\bar{\phi}\frac{\partial\phi}{\partial n} - \phi\frac{\partial\bar{\phi}}{\partial n}) = 0,$$

that is zero because of the periodicity boundary conditions at the boundary δD of

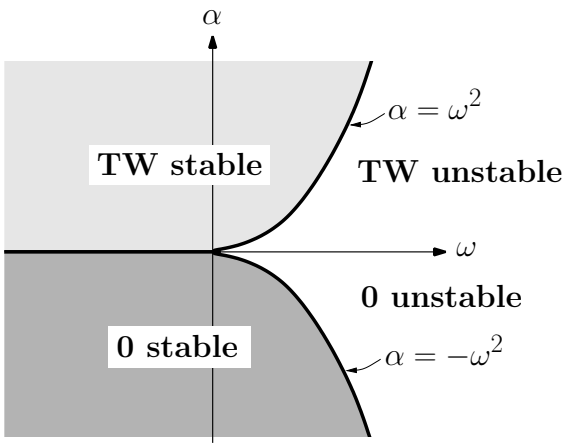

Figure 5: Stability diagram for the zero solution and the TW. Light shading: TW stable. Dark shading: zero solution stable.

the square domain D. The same arguments allow us to write

$$\int_D (\bar{\phi}\nabla^2\phi + \phi\nabla^2\bar{\phi}) = -2\int_D |\nabla\phi|^2,$$

and

$$\int_D (\bar{\phi}\nabla^4\phi + \phi\nabla^4\bar{\phi}) = 2\int_D |\nabla^2\phi|^2,$$

where we have also make use of the relation

$$\bar{\phi}\nabla^4\phi = \nabla\cdot(\bar{\phi}\nabla(\nabla^2\phi) - (\nabla\bar{\phi})(\nabla^2\phi)) + |\nabla^2\phi|^2.$$

Collecting all the above results, one can write

$$\frac{d}{dt}\int_D |\phi|^2 = 2[\int_D |\phi|^2(\alpha - |\phi|^2) + 2\varepsilon\omega\int_D |\nabla\phi|^2 - \varepsilon^2\int_D |\nabla^2\phi|^2], \tag{21}$$

and also

$$\frac{d}{dt}\int_D |\phi|^2 = 2[\int_D |\phi|^2(\alpha + \omega^2 - |\phi|^2) - \int_D |\varepsilon\nabla^2\phi + \omega\phi|^2], \tag{22}$$

as it can be readily seen after taking into account the following relation

$$|\varepsilon\nabla^2\phi + \omega\phi|^2 = \varepsilon^2|\nabla^2\phi|^2 + \omega^2|\phi|^2 + \varepsilon\omega(\bar{\phi}\nabla^2\phi + \phi\nabla^2\bar{\phi})$$

and the result above for the integral of its last term.

Finally, for $\omega < 0$ all negative terms in the right hand side of eq. (21) can be removed to give

$$\frac{d}{dt}\int_D |\phi|^2 \leq 2\alpha \int_D |\phi|^2,$$

that, according to Gronwall's Lemma, implies that

$$\int_D |\phi|^2 \leq C\mathrm{e}^{2\alpha t} \to 0 \quad \text{as} \quad t \to \infty,$$

and thus we can conclude that

$$\int_D |\phi|^2 \to 0 \quad \text{as} \quad t \to \infty,$$

i.e., all solutions decay to zero for $\alpha < 0$ and $\omega < 0$. If now $\omega > 0$, then we can use Eq. (22) and follow the same argumentation as above to obtain that, for $\alpha + \omega^2 < 0$, all solutions also decay to zero.

It is interesting to notice that the global stability of the zero solution allow us to conclude that the CSH cannot exhibit localized solutions with a nonzero central core and tail that decays to zero; in order to have such solutions the zero solution has to be stable but this also implies, because of the global stability, that the pulse-like solution has to decay to zero.

4.1 TW solutions

The simplest nonzero solutions of the CGL eq. (18) are the spatially uniform travelling waves (TW),

$$\phi_{\mathrm{TW}} = \sqrt{\alpha}\, \mathrm{e}^{\mathrm{i}\mathbf{k}_{\mathrm{TW}}\cdot\mathbf{x} - \mathrm{i}k_{\mathrm{TW}}^2 t}, \tag{23}$$

with $k_{\mathrm{TW}} = |\mathbf{k}_{\mathrm{TW}}| \sim 1$, which exist only for $\alpha > 0$ and are approximate solutions of the CSH up to $\mathcal{O}(\varepsilon)$ corrections.

The TW stability characteristics can be easily obtained looking for solutions of the form

$$\phi = \phi_{\mathrm{TW}}(1 + \xi) \quad \text{with} \quad |\xi| \ll 1$$

in the CSH and neglecting all but the linear terms. The following equation for the

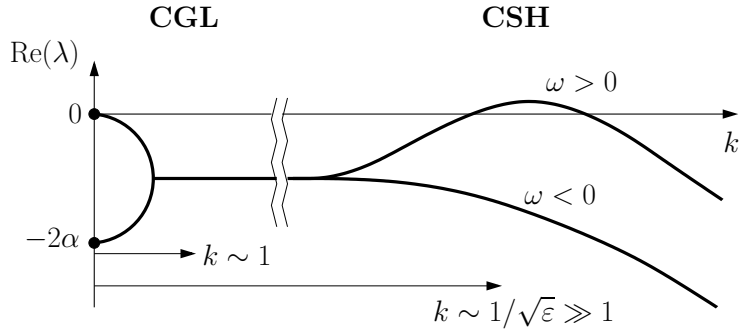

Figure 6: Growth rate of the perturbations of the TW for $\omega > 0$ and $\omega < 0$, with the two wavenumber regions shown: $k \sim 1$ (dispersive perturbations) and $k \sim 1/\sqrt{\varepsilon} \gg 1$ (diffusive perturbations).

evolution of the perturbation ξ is obtained

$$\xi_t = \mathrm{i}(\nabla^2\xi + \mathrm{i}2\mathbf{k}_{\mathrm{TW}} \cdot \nabla\xi) - \alpha(\xi + \bar{\xi}) - 2\varepsilon\omega[\nabla^2\xi + \dots] - \varepsilon^2[\nabla^4\xi + \dots],$$

where, as we will see below, only the main contribution of the small diffusive terms needs to be retained. If we now expand ξ in Fourier series

$$\xi = \sum \xi_{\mathbf{k}}(t)\mathrm{e}^{\mathrm{i}\mathbf{k}\cdot\mathbf{x}},$$

only the mode pairs with wavevectors $\pm\mathbf{k}$ are coupled and their evolution equations read

$$\frac{d\xi_{\mathbf{k}}}{dt} = (-\alpha - \mathrm{i}k^2 - \mathrm{i}2\mathbf{k}_{\mathrm{TW}} \cdot \mathbf{k} + 2\varepsilon\omega k^2 - \varepsilon^2 k^4)\xi_{\mathbf{k}} - \alpha\bar{\xi}_{-\mathbf{k}},$$
$$\frac{d\bar{\xi}_{-\mathbf{k}}}{dt} = (-\alpha + \mathrm{i}k^2 - \mathrm{i}2\mathbf{k}_{\mathrm{TW}} \cdot \mathbf{k} + 2\varepsilon\omega k^2 - \varepsilon^2 k^4)\bar{\xi}_{-\mathbf{k}} - \alpha\xi_{\mathbf{k}}.$$

where $k = |\mathbf{k}|$. The solutions of this linear system are proportional to $\mathrm{e}^{\lambda t}$ with λ given by

$$\lambda = -\alpha - \mathrm{i}2\mathbf{k}_{\mathrm{TW}} \cdot \mathbf{k} + 2\varepsilon\omega k^2 - \varepsilon^2 k^4 \pm \sqrt{\alpha^2 - k^4}.$$

Again, we can distinguish between perturbations exhibiting only dispersive scales, i.e., with wavevector $|\mathbf{k}| \sim 1$, which have a growth rate that can be approximated as

$$\mathrm{Re}(\lambda) = -\alpha \pm \sqrt{\alpha^2 - k^4} + \dots \tag{24}$$

and are always stable because α is positive for all TW (see Fig. 6); this is again the result that is obtained if the linear stability analysis is performed on the CGL. And perturbations with high diffusive wavevectors, $k \sim K/\sqrt{\varepsilon} \gg 1$, whose dynamics is not contained in the CGL, and their growth rate, up to $\mathcal{O}(\sqrt{\varepsilon})$ corrections, is given by

$$\mathrm{Re}(\lambda) = -\alpha + 2\omega K^2 - K^4 + \ldots, \tag{25}$$

which is also plotted in Fig. 6. These diffusive, short wave perturbations become unstable outside the region defined by $\omega > 0$ and $\alpha > \omega^2$ (marked with light shading in Fig. 5) with critical wavenumber $k = \sqrt{\omega}/\sqrt{\varepsilon} \gg 1$. Note that the growth rate of the diffusive perturbations is of order one and thus this not a higher order correction that evolves on a much slower time scale; this instability develops in the time scale $t \sim 1$ of the dispersive CGL dynamics.

Finally, it is also interesting to mention that the region $\omega > 0$ and $-\omega^2 < \alpha < \omega^2$ in Fig. 5 appears to be the best suited to look for complex dynamics because in there both the zero solution and the uniform TW are unstable.

4.2 Spirals

The rotating spiral wave solutions of the CGL are of the form

$$\phi_{\mathrm{S}} = \sqrt{\alpha}\,\rho(r)\,\mathrm{e}^{\mathrm{i}(\omega_{\mathrm{S}} t + m\theta + \psi(r))},$$

where (r, θ) are polar coordinates, $m \in \mathbb{N}$ represents the number of arms of the spiral and ω_{S} its rotating angular frequency. After inserting the expression above into the CGL eq. (18), the following equations are obtained for the functions $\rho(r)$ and $\psi(r)$

$$\rho_{rr} + \frac{1}{r}\rho_r - \rho(\psi_r^2 + \frac{m^2}{r^2}) = \omega_{\mathrm{S}}\rho, \tag{26}$$

$$\psi_{rr} + \frac{1}{r}\psi_r + 2\frac{\rho_r}{\rho}\psi_r = 1 - \rho^2, \tag{27}$$

together with the following boundary conditions that prevent the formation of singularities at $r = 0$

$$\psi_r(0) = 0, \quad \rho(r) = \rho_0 r^m \quad \text{for} \quad r \to 0, \quad \text{and} \quad \rho(r) \to 1 \quad \text{for} \quad r \to \infty, \tag{28}$$

see e.g. [24]. The spiral is zero at the origin and, as $r \to \infty$, its amplitude approaches that of the uniform TW $\sqrt{\alpha}$ and its radial wavenumber verifies

$$\psi_r \to \psi_{r\infty}, \quad \text{with} \quad \omega_{\rm S} = -\psi_{r\infty}^2,$$

which is precisely the frequency-wavenumber relation of the TW. These spirals of the CGL are again solutions of the CSH up to $\mathcal{O}(\varepsilon)$ error.

The numerical integration of the semi-infinite, singular boundary value problem (26)-(28) has been performed following the steps below.

1. In order to avoid the singularity at $r = 0$, the solution at $r = r_0 \ll 1$ is approximated by the expansions for $r \to 0$

$$\rho(r) = \rho_0 r^m + \frac{\rho_0 \omega_{\rm S}}{4(m+1)} r^{m+1} + \dots,$$
$$\psi_r(r) = \frac{r}{2(m+1)} + \dots.$$

2. The third order system (26)-(27) for (ρ_r, ρ, ψ_r) is now integrated from $r = r_0$ to $r = r_\infty \gg 1$ and, at $r = r_\infty$, the solution is forced to match the expansion for $r \to \infty$

$$\rho(r) = 1 - \frac{\psi_{r\infty}}{2r} - \frac{5\psi_{r\infty}^2}{8r^2} - \frac{4m^2 + 29\psi_{r\infty}^4}{16\psi_{r\infty} r^3} - \frac{80m^2 + 973\psi_{r\infty}^4 + 32}{128 r^4} + \dots.$$

3. For every fixed value of m, the matching conditions for ρ and ρ_r at $r = r_\infty$ give of a two equation system for $\omega_{\rm S}$ and ρ_0 that is solved applying Newton's method (with the Jacobian approximated using second order finite differences). Note that there is no need to match ψ_r since it is completely defined, once ρ is known, by the expression

$$\psi_r(r) = \frac{1}{r\rho^2(r)} \int_0^r s\rho^2(s)(1 - \rho^2(s))\, ds,$$

which is readily obtained from eq. (27) after multiplying by $r\rho^2$ and integrating from 0 to r.

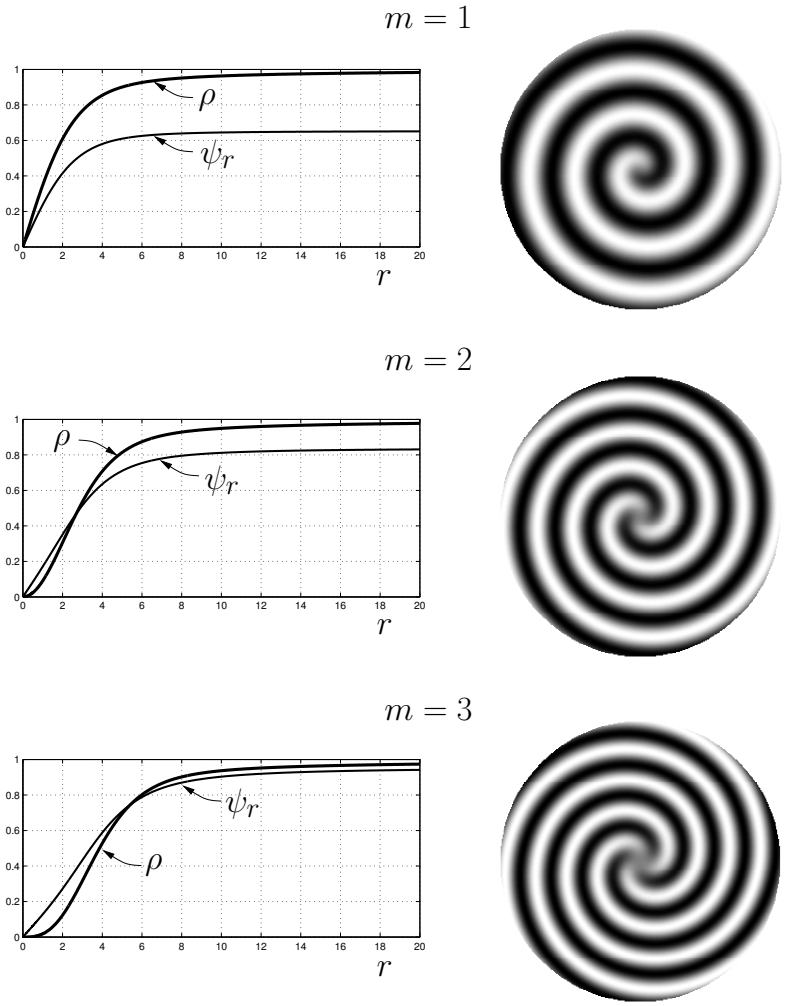

Figure 7: From top to bottom: one, two and three armed spiral solutions corresponding to $m = 1, 2$ and 3. The left column shows the amplitude ρ and radial wavenumber ψ_r profiles. Right column shows the grayscale map of the real part of $\phi_{\rm S}$.

The resulting spirals for $m = 1, 2$ and 3 are shown in in Fig. 7, and the corresponding values of ρ_0 and the rotating frequency $\omega_{\rm S}$ are given in the table below.

m	$\omega_{\rm S}$	ρ_0
1	-0.426468	0.365958
2	-0.700454	0.0957711
3	-0.909445	0.0192913

The computations have been done for $r_0 = 10^{-3}$ and $r_\infty = 20$ in order to ensure that the errors in the expansions for $r \to 0$ and $r \to \infty$ above, which are $\sim r_0^2$ and $\sim 1/r_\infty^5$ respectively, are both below 10^{-6} (we have also checked that the digits presented in the table do not change when r_0 is reduced to 10^{-4} and r_∞ is increased to 30).

5 Numerical results

The purpose of the numerical results presented in this section is twofold: (i) We will first perform some numerical simulations of the order parameter equation (the CSH eq. (17)) to check the stability predictions of the previous section and to show, as it was advanced in Section 3, the presence of two essentially different scales in the extended system limit $\varepsilon \to 0$, namely, dispersive, $\delta_{\text{disp}} \sim 1$, and diffusive scales, $\delta_{\text{diff}} \sim \sqrt{\varepsilon}$. And (ii) we will then numerically integrate both, the complete MB eqs. (1)-(3) and the CSH eq. (17), and compare their respective solutions to confirm the validity of the CSH as the appropriate order parameter equation for the description of the weakly nonlinear dynamics of the MB.

5.1 Numerical simulations of the CSH

The CSH equation (17) is numerically integrated in a square domain $[0, 1] \times [0, 1]$ with periodic boundary conditions for four representative sets of parameter values.

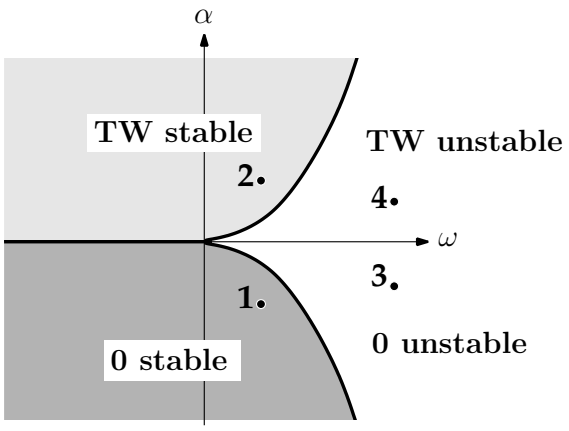

Figure 8: Stability diagram for the zero solution and the TW. Light shading: TW stable. Dark shading: zero solution stable. Numbered dots correspond to the parameter values used in the numerical integrations.

CASE 1: $\alpha = -0.75$ and $\omega = 0.5$. For these parameter values, the results obtained in Section 4 indicate that the zero solution is globally stable, see Fig. 8. The initial condition used in all simulations is a constant amplitude pure mode with

wavevector $\mathbf{k}_{\mathrm{TW}} = (1, 2)$, represented in Fig. 9, and with a superimposed random perturbation of amplitude 10^{-3}. The CSH has been integrated for three different values of ε and the resulting time evolution of the norms of the solution

$$||\phi|| = \sqrt{\int_0^1 \int_0^1 |\phi| \, dx \, dy} \quad \text{and} \quad ||\nabla\phi|| = \sqrt{\int_0^1 \int_0^1 ||\nabla\phi|| \, dx \, dy}$$

are shown in Fig. 10. As it was expected, the dynamics of the system in this case is extremely simple, and all three solutions decay to zero. It is interesting to notice that the decay rate for $\varepsilon \ll 1$ appears to be independent of ε (see the slopes of the two solid lines in the lower plot in Fig. 10) but different from that for $\varepsilon = 0$ (dashed line in the lower plot in Fig. 10), which decays faster. This is also in agreement with the results from Section 4: the dispersion relation of the zero solution for $\varepsilon \ll 1$ is given by eq. (20), whose maximum value $\alpha - \omega^2 = -0.5$ (associated to the slowest decaying modes) is independent of ε and different form that corresponding to $\varepsilon = 0$ (when the CSH equation simplifies to the the CGL equation (18)) that, according to eq. (19), is constant and equal to $\alpha = -0.75$, and thus produces a faster decay to zero.

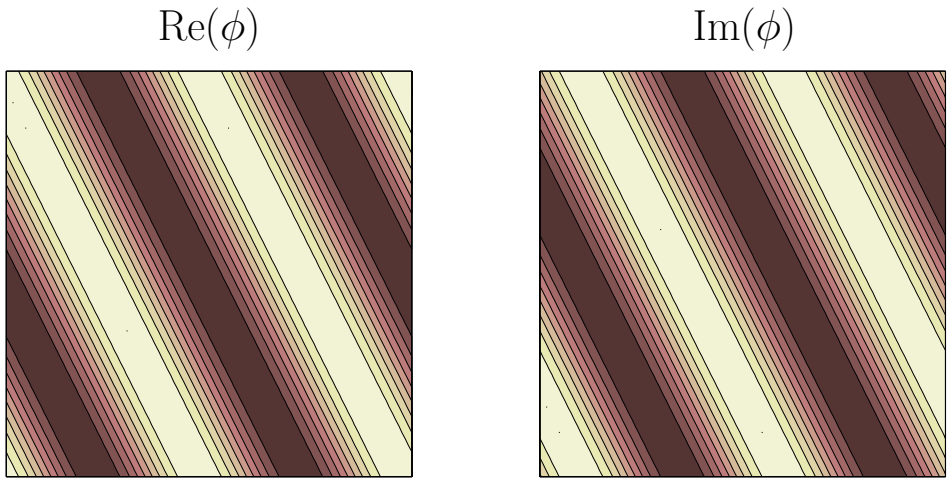

Figure 9: Colored contour maps of the real (left) and imaginary (right) part of a pure mode field of the form $\phi = \sqrt{|\alpha|}\mathrm{e}^{\mathrm{i}\mathbf{k}\cdot\mathbf{x}}$ with $\alpha = -0.75$ and $\mathbf{k}_{\mathrm{TW}} = (1, 2)$. Lighter (darker) colors correspond to higher (lower) values.

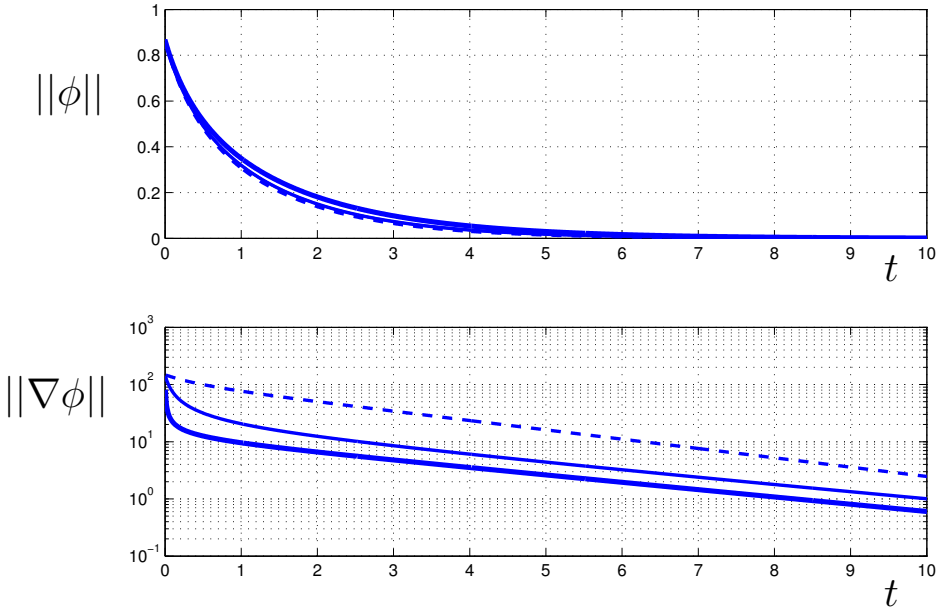

Figure 10: Time evolution of the norm of the solution of the CSH eq. (17) (above) and its gradient (below). The initial condition is the pure mode in Fig 9 with a random perturbation of size 10^{-3}, and the parameters correspond to the CASE 1 in Fig. 8 with $\varepsilon = 10^{-3}$ (thick line), $\varepsilon = 10^{-3}/4$ (thin line) and $\varepsilon = 0$ (CGL eq. (18), dashed line).

CASE 2: $\alpha = 0.75$ and $\omega = 0.5$. We are now in the region of the parameter space where the uniform TW described by expression (23) in Section 4.1 are all stable (see Fig. 8). Recall that these are TW with wavenumber $k \sim 1$ (without diffusive scales) and therefore, in the $\varepsilon \ll 1$ limit, they are approximately given by the CGL equation (18). The starting point of the numerical integrations shown in Fig. 11 is now a uniform TW (i.e. that with $\mathbf{k}_{\rm TW} = (0, 0)$ and amplitude $\sqrt{\alpha}$) with a 10^{-3} random perturbation, and, as expected, the system relaxes to the uniform TW: $||\phi|| \to \sqrt{\alpha}$ and $||\nabla\phi|| \to 0$. As it can be appreciated from the lower plot of Fig. 11, the resulting decay rate for $\varepsilon \ll 1$ is again independent of ε and is given by the maximum of the growth rate (25), $-\alpha + \omega^2 = -0.5$, and it again differs from that for $\varepsilon = 0$ that, according to expression (24), is equal to $-\alpha = -0.75$.

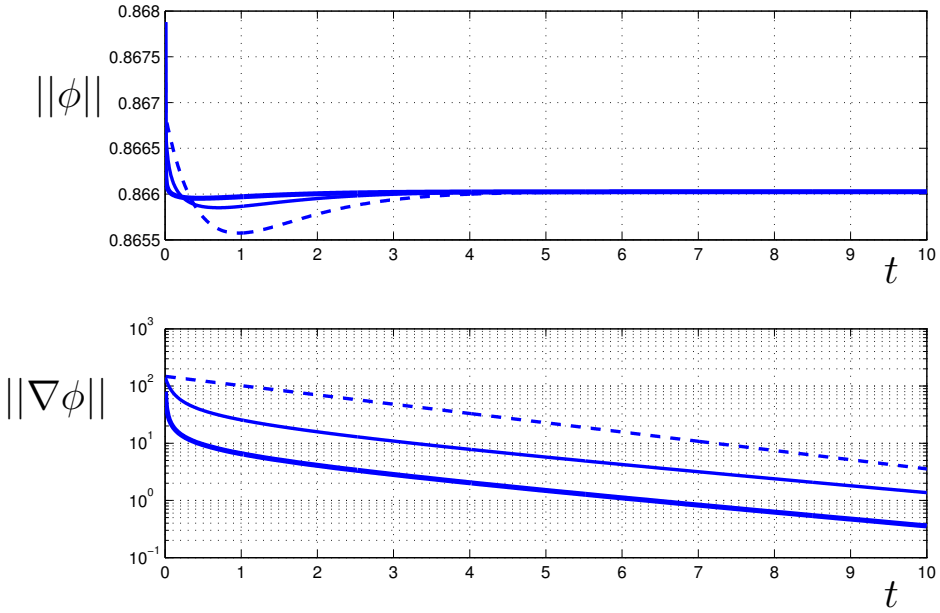

Figure 11: Time evolution of the norm of the solution of the CSH eq. (17) (above) and its gradient (below). The initial condition is a spatially uniform steady solution with a random perturbation of size 10^{-3}, and the parameters correspond to the CASE 2 in Fig. 8 with $\varepsilon = 10^{-3}$ (thick line), $\varepsilon = 10^{-3}/4$ (thin line) and $\varepsilon = 0$ (CGL eq. (18) dashed line).

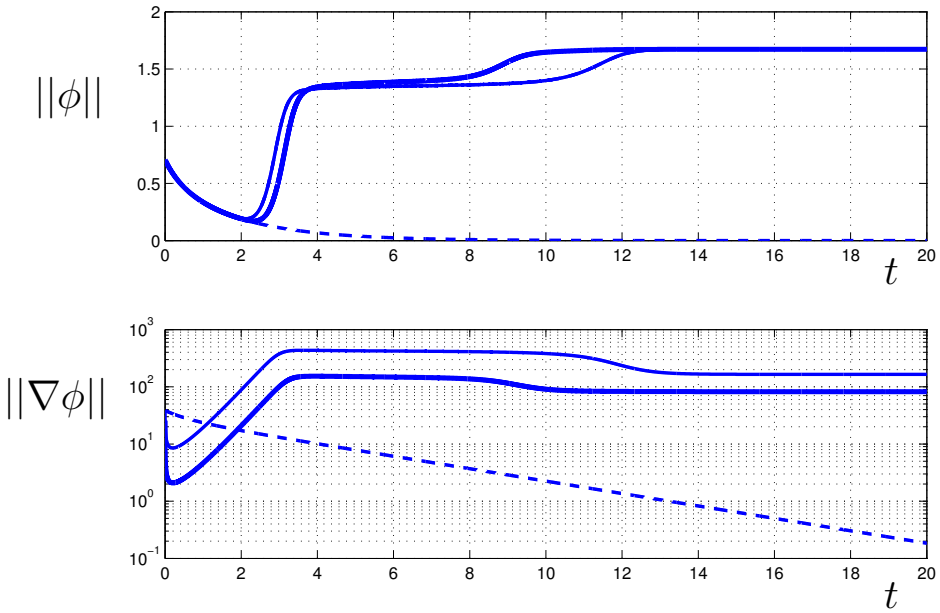

Figure 12: Time evolution of the norm of the solution of the CSH eq. (17) (above) and its gradient (below). The initial condition is a spatially uniform steady solution with a random perturbation of size 10^{-3}, and the parameters correspond to the CASE 3 in Fig. 8 with $\varepsilon = 10^{-3}$ (thick line), $\varepsilon = 10^{-3}/4$ (thin line) and $\varepsilon = 0$ (CGL eq. (18), dashed line).

CASE 3: $\alpha = -0.5$ and $\omega = 2$. The initial condition is the same perturbed uniform state used in CASE 2, but now, as it is clear from Fig. 12, the behaviour of the system for $\varepsilon \ll 1$ is completely different from that for $\varepsilon = 0$. The resulting temporal evolution for $\varepsilon = 0$ is just a monotonous decay to the zero solution (dashed line in Fig. 12) that, according to eq. (19), is always stable in the CGL dynamics when α is negative. On the other hand, the zero solution is unstable for the CSH with $\varepsilon \ll 1$ (see Fig. 8), and what happens now is that the system evolves to a nonzero final state that exhibits small diffusive scales (solid lines in Fig. 12). These small diffusive scales grow exponentially with a finite non-zero growth rate as $\varepsilon \to 0$, see the lower plot of Fig. 12. Note that, despite of the small coefficients of diffusion and double diffusion in the CSH eq. (17), the onset of these small diffusive scales is not a higher order, longer time scale effect; they evolve in the $t \sim 1$ time scale of the CSH, as it is clear from the slope of the solid lines in the lower plot of Fig. 12. The resulting values of $||\nabla\phi||$ at $t = 20$ for $\varepsilon = 10^{-3}$ and $\varepsilon = 10^{-3}/4$ are, respectively, 82.187 and 164.85, whose ratio is equal to $2.006\ldots$, in agreement with the fact that the small diffusive scales dominate the final state, forcing the norm of the gradient to behave, in first approximation, as $||\nabla\phi|| \sim 1/\sqrt{\varepsilon}$. Moreover, the solutions at $t = 20$ for $\varepsilon = 10^{-3}$ and $\varepsilon = 10^{-3}/4$ (shown in Figs. 13 and 14) resemble a TW with a number of wavelengths that is roughly 7 and 14, indicating that this final state corresponds to a TW but with a diffusive wavenumber $k \sim 1/\sqrt{\varepsilon}$.

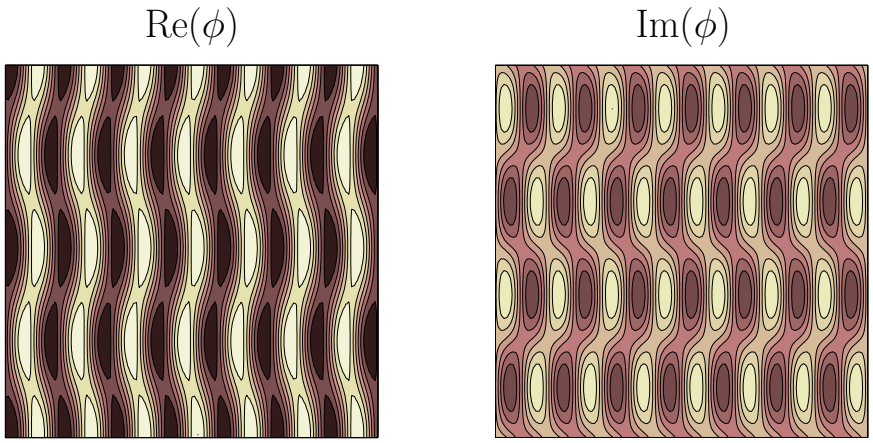

Figure 13: Colored contour maps of the real (left) and imaginary (right) part of the solution of the CSH eq. (17) at $t = 20$ for $\alpha = -0.5$, $\omega = 2$ and $\varepsilon = 10^{-3}$.

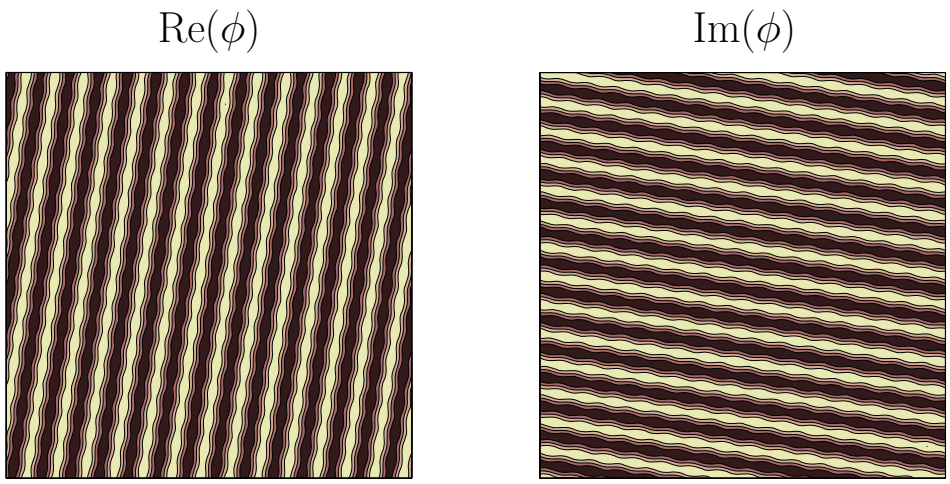

Figure 14: Colored contour maps of the real (left) and imaginary (right) part of the solution of the CSH eq. (17) at $t = 20$ for $\alpha = -0.5$, $\omega = 2$ and $\varepsilon = 10^{-3}/4$.

CASE 4: $\alpha = 0.5$ and $\omega = 2$. The initial condition is now that of the CASE 1 simulations: a TW with wavevector $\mathbf{k}_{\rm TW} = (1, 2)$ shown in Fig. 9 with a 10^{-3} perturbation. This TW is stable in the CGL dynamics; this is clearly seen in the results for $\varepsilon = 0$ plotted in Fig. 15, where the norm of the solution remains almost constant and equal to its initial value $\sqrt{\alpha}$, and the perturbations (lower plot) decay exponentially. As it happened in the previous case, this TW is unstable for the CSH with $\varepsilon \ll 1$, and the solution develops small diffusive scales that grow exponentially (see the solid lines in Fig. 15). The ratio of the final values of $||\nabla\phi||$ for $\varepsilon = 10^{-3}$ and $\varepsilon = 10^{-3}/4$ is approximately $176.2/87.6 = 2.01$, and there are twice as much wavelengths in the solution in Fig. 17 for $\varepsilon = 10^{-3}/4$ than in that shown in Fig. 16 for $\varepsilon = 10^{-3}$, indicating again that the final state is a TW with diffusive wavenumber $k \sim 1/\sqrt{\varepsilon}$. Notice that this TW is very similar to that obtained in the previous case; this is due to the fact that the most unstable wavenumber is given by $k \sim \sqrt{\omega}/\sqrt{\varepsilon}$ (see eq.(25)) that depends only on ω and ε, which take the same values in both cases (the amplitude of both TW is different but this cannot be appreciated in the color maps).

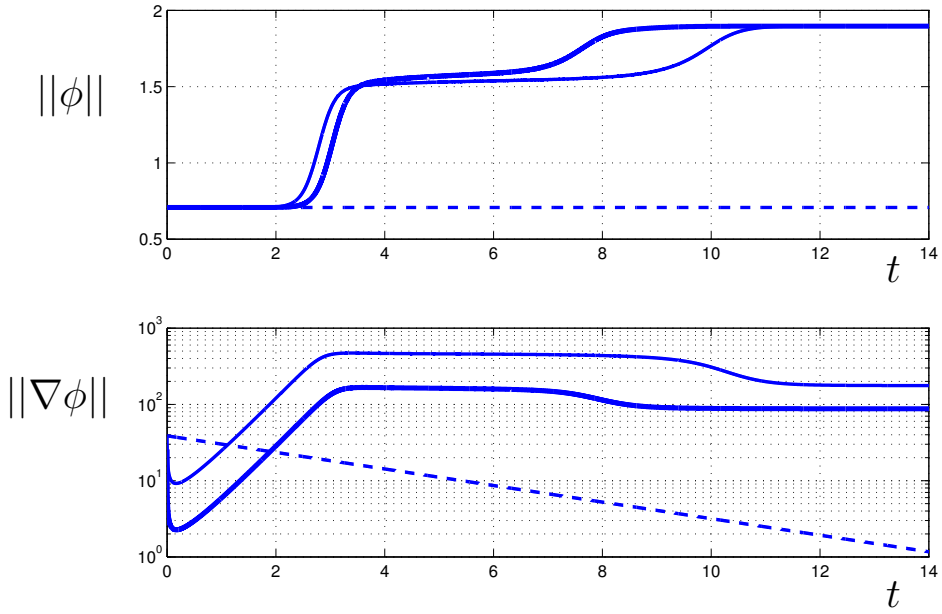

Figure 15: Time evolution of the norm of the solution of the CSH eq. (17) (above) and its gradient (below). The initial condition is a spatially uniform steady solution with a random perturbation of size 10^{-3}, and the parameters correspond to the CASE 4 in Fig. 8 with $\varepsilon = 10^{-3}$ (thick line), $\varepsilon = 10^{-3}/4$ (thin line) and $\varepsilon = 0$ (CGL eq. (18), dashed line).

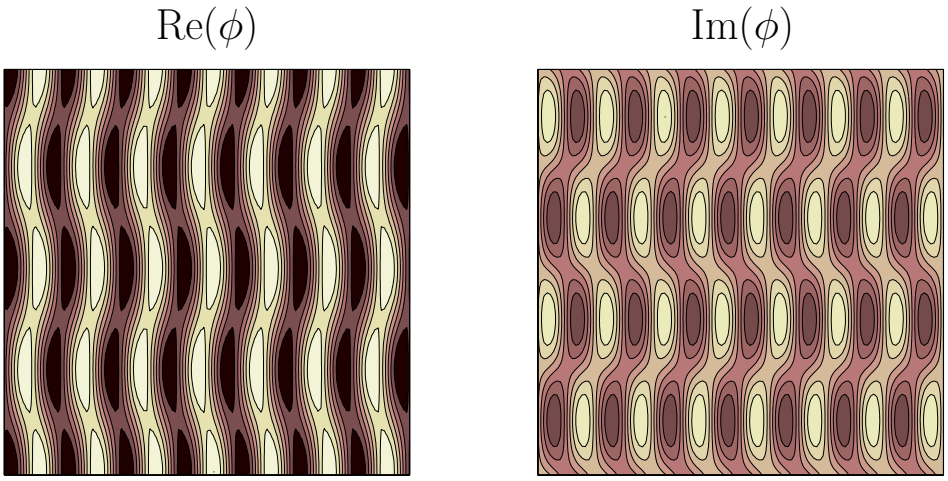

Figure 16: Colored contour maps of the real (left) and imaginary (right) part of the solution of the CSH eq. (17) at $t = 20$ for $\alpha = 0.5$, $\omega = 2$ and $\varepsilon = 10^{-3}$.

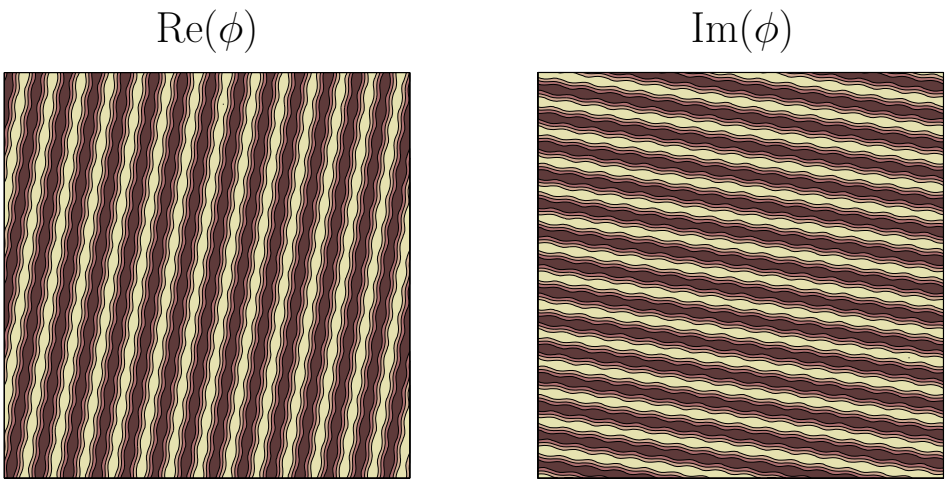

Figure 17: Colored contour maps of the real (left) and imaginary (right) part of the solution of the CSH eq. (17) at $t = 20$ for $\alpha = 0.5$, $\omega = 2$ and $\varepsilon = 10^{-3}/4$.

The numerical simulations presented above clearly show that there are two types of solutions of the CSH with a completely different behaviour in the physically relevant limit of large systems $\varepsilon \to 0$: those that only exhibit scales that are of the order of the total size of the domain, $\delta_{\text{disp}} \sim 1$, and that can be accurately approximated by the simpler CGL that is obtained by setting $\varepsilon = 0$ in the CSH (CASES 1 and 2), and those that develop small diffusive scales, $\delta_{\text{diff}} \sim \sqrt{\varepsilon}$, whose dynamics can only be correctly described using the CSH with $\varepsilon \ll 1$ (CASES 3 and 4).

The details of the applied numerical scheme are given below in section 5.4. The typical number of Fourier modes used in the simulations above are 64×64 and 128×128, with a time step in the range $dt = 0.001 \ldots 0.0001$.

5.2 MB and CSH solution comparison

In this section we numerically check the accuracy of the CSH eq. (17) as the order parameter equation for the description of the weakly nonlinear dynamics of the MB eqs. (1)-(3) with small detuning.

We numerically integrate the MB in a large square domain $[0, L] \times [0, L]$ with

periodic boundary conditions and $L \gg 1$. The pump and the detuning are taken appropriately small

$$|r-1| \sim \frac{1}{L^2} \ll 1 \quad \text{and} \quad |\Omega| \sim \frac{1}{L} \ll 1,$$

and the initial condition, according to the scaling in (16), takes the form

$$\begin{bmatrix} E \\ P \\ N \end{bmatrix}_0 = \sqrt{\frac{b}{\sigma}} \begin{bmatrix} 1 \\ 1 \\ 0 \end{bmatrix} \frac{\phi_0(x/L, y/L)}{L} \ll 1,$$

where b and σ are fixed, order one parameters (class C laser), and the complex function ϕ_0 is periodic in $[0,1]\times[0,1]$ and such that $|\phi_0| \sim 1$, and the final integration time t_{MB} is chosen such that

$$t_{\mathrm{MB}} \sim L^2 \gg 1.$$

We also integrate the CSH in the domain $[0,1] \times [0,1]$ with periodic boundary conditions, $\phi_0(x,y)$ as initial condition and the following parameters (see (16))

$$\alpha = L^2\sigma((r-1) - \frac{\Omega^2}{(\sigma+1)^2}) \sim 1, \tag{29}$$

$$\omega = L\Omega\frac{\sqrt{\sigma}}{\sigma+1} \sim 1, \tag{30}$$

$$\varepsilon = \frac{\sqrt{\sigma}}{\sigma+1}\frac{1}{L} \ll 1, \tag{31}$$

and up to a final time

$$t_{\mathrm{CSH}} = \frac{1}{(\sigma+1)L^2} t_{\mathrm{MB}}. \tag{32}$$

In order to quantitatively measure the accuracy of the order parameter description, we first perform several simulations of the MB with increasing domain size and final time

MB_1	MB_2	MB_3	$\dots$
L_1	L_2	L_3	$\dots$
t_{MB_1}	t_{MB_2}	t_{MB_3}	$\dots$
$r_1 - 1$	$r_2 - 1$	$r_3 - 1$	$\dots$
Ω_1	Ω_2	Ω_3	$\dots$

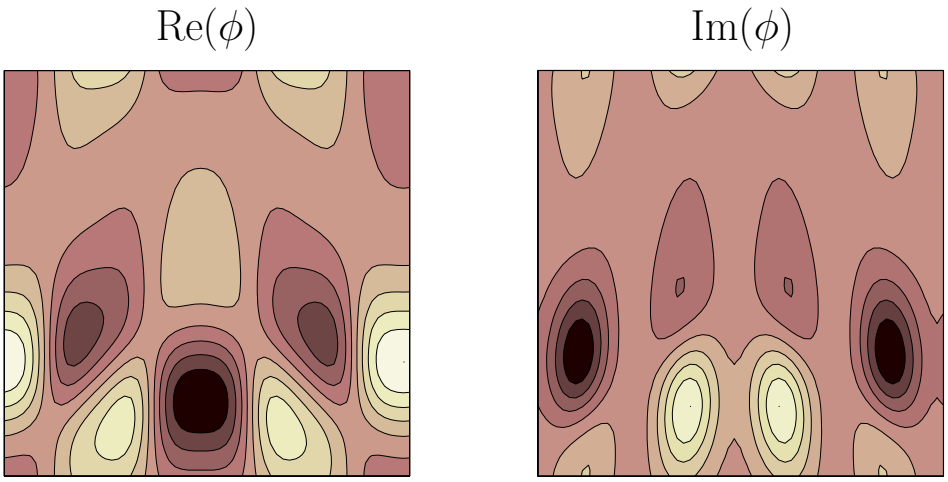

Figure 18: Colored contour maps of the real (left) and imaginary (right) part of the initial condition used for the CSH and MB comparison.

and the corresponding ones of the CSH

CSH_1	CSH_2	CSH_3	...
ε_1	ε_2	ε_3	...

keeping fixed b, σ, α, ω and the final CSH integration time, t_{CSH}, and obtaining the rest of the parameters $(r_i - 1)$, Ω_i, t_{MB_i} and ϵ_i from the above eqs. (29)-(32) for every given value of L_i. And then, we evaluate the difference of both solutions

$$d_i(t) = \| \begin{bmatrix} E \\ P \\ N \end{bmatrix}_{\mathrm{MB}_i} (L^2(\sigma+1)t) - \sqrt{\frac{b}{\sigma}} \begin{bmatrix} 1 \\ 1 \\ 0 \end{bmatrix} \frac{\phi_{\mathrm{CSH}_i}(x/L_i, y/L_i, t_{\mathrm{CSH}_i})}{L_i} \mathrm{e}^{-\mathrm{i}\frac{\sigma\Omega_i}{(\sigma+1)}t} \|, \quad (33)$$

and check the asymptotic behavior predicted in section 3,

$$d_i/\varepsilon_i \to 0 \quad \text{as} \quad \varepsilon_i \to 0. \quad (34)$$

We repeat the above procedure for two sets of parameter values:

CASE 1: $\sigma = 1$, $b = 1$, $\alpha = 0.75$ and $\omega = 0.5$. The initial condition (plotted in Fig. 18) is given by the expression

$$\phi_0(x, y) = 0.5 + 3\mathrm{i} + \cos(x + \cos y)\mathrm{e}^{\sin x + \mathrm{i}3\cos^2 y},$$

which presents several peaks and valleys and has been selected in order to ensure that the simulations are started at a generic state, away from the simple TW solutions. Both systems have been integrated up to final time $t_{\rm CSH} = 10$ and for four different values of L, with parameters

	$\rm MB_1$	$\rm MB_2$	$\rm MB_3$	$\rm MB_4$
L	20	30	40	50
$t_{\rm MB}$	8000	18000	32000	50000
$r-1$	0.0025	0.001111...	0.000625	0.0004
Ω	0.05	0.03333...	0.025	0.02

	$\rm CSH_1$	$\rm CSH_2$	$\rm CSH_3$	$\rm CSH_4$
ε	0.025	0.01666...	0.0125	0.01

And the resulting MB-CSH differences (33) are shown in Fig. 19. The time evolution of the MB presents a short initial stage, that takes place for $t_{\rm MB} \sim 1$ ($t_{\rm CSH} \sim 1/L^2 \ll 1$), in which the system quickly damps out all modes with high wavenumber. This produces a sharp growth and decrease of the MB-CSH difference that can be appreciated in the lower left plot of Fig. 19. After this initial phase, the system enters the slow dynamics regime and its evolution takes place in the scale $t_{\rm CSH} \sim 1$ ($t_{\rm CSH} \sim L^2 \gg 1$), see top plot of Fig. 19. The maximum values of each difference, $d_{\rm max}$, divided by ε are plotted against ε in the lower right plot of Fig. 19; it is clear from this plot that $d_{\rm max}/\varepsilon$ goes to zero as ε is decreased, confirming the asymptotic behavior predicted in (34).

CASE 2: $\sigma = 1$, $b = 1$, $\alpha = 0.5$ and $\omega = 2$. The initial condition is that of the previous case and, again, both systems have been integrated up to final time $t_{\rm CSH} = 10$, but now for five different values of L, with parameters

	$\rm MB_1$	$\rm MB_2$	$\rm MB_3$	$\rm MB_4$	$\rm MB_5$
L	20	30	40	50	60
$t_{\rm MB}$	8000	18000	32000	50000	72000
$r-1$	0.01125	0.005	0.0028125	0.0018	0.00125
Ω	0.2	0.1333...	0.1	0.08	0.06666...

	$\rm CSH_1$	$\rm CSH_2$	$\rm CSH_3$	$\rm CSH_4$	$\rm CSH_5$
ε	0.025	0.01666...	0.0125	0.01	0.008333...

and the results are now presented in Fig. 20. Again the system exhibits a fast adaptation stage (lower left plot of Fig. 20) followed by a slow evolution in the

$t_{\rm CSH} \sim 1$ time scale (top plot of Fig. 20). But now, we are in a point of the parameter space where the final state exhibits diffusive scales $\delta_{\rm diff} \sim \sqrt{L}$ in the MB variables. And thus, it is now necessary to go to higher L values ($L > 50$, $\varepsilon < .01$) in order to have a clear separation of scales between $\delta_{\rm disp} \sim L$ and $\delta_{\rm diff} \sim \sqrt{L}$ ($\delta_{\rm disp} \sim 1$ and $\delta_{\rm diff} \sim \sqrt{\varepsilon}$ in the CSH scaling) and start to see the asymptotic decay predicted in (34), see the dots in the bottom right plot of Fig. 20.

The numerical method used to integrate the MB eqs. (1)-(3) is briefly described in the following section. The computations above have been carried out with 64×64 Fourier modes and time integration step $dt = 0.0025$ and $dt = 0.00125$. Note that such small time steps are necessary in order to be sure that the numerical integration errors of the MB equations are kept small and do not contaminate the differences that we trying to compute. The combination of small time steps ($dt = 0.0025$) and very long integration times ($t_{\rm MB} = 50000$) makes the computations presented above extremely CPU costly; the computation of the time evolution of one MB-CSH difference may take up to 5 days in a 3GHz Pentium IV computer with 1Gb RAM.

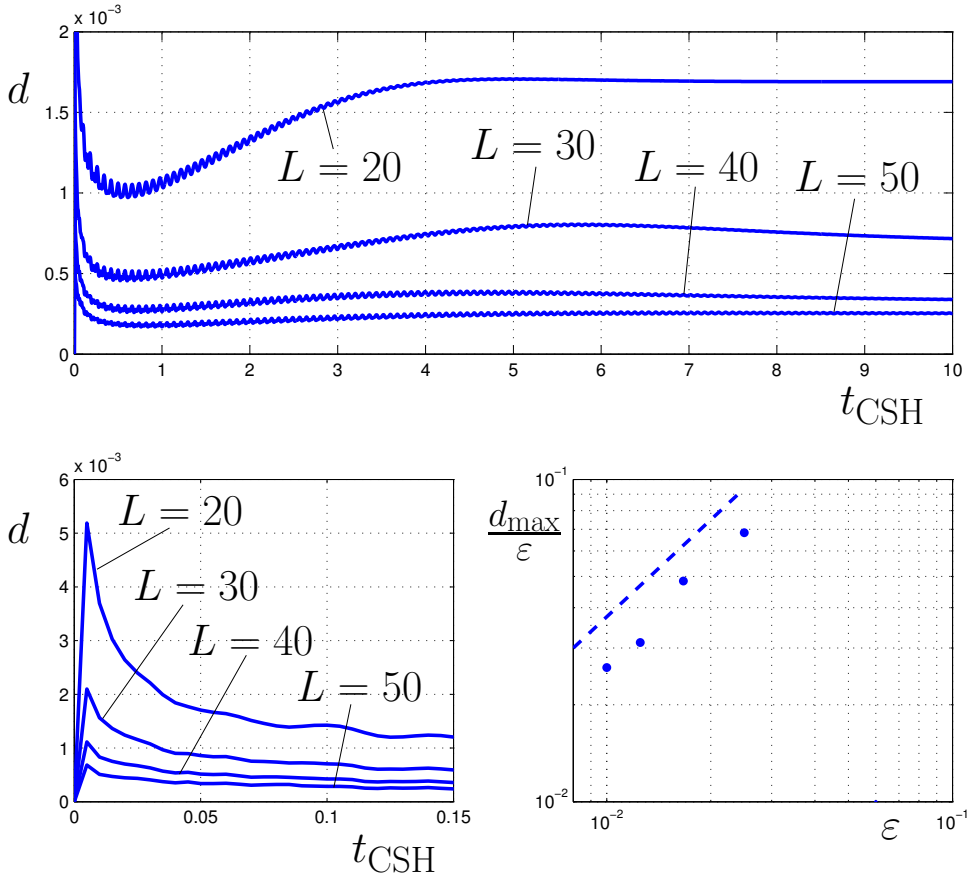

Figure 19: Top plot: Time evolution of the difference of the solution of the CSH and MB equations for $\sigma = 1$, $b = 1$, $\alpha = 0.75$, $\omega = 0.5$ and $L = 20, 30, 40$ and 50. Bottom plot: short time detail of evolution of difference (left) and (right) the resulting maximum values of the difference versus ε (the dashed line corresponds to a decay $\frac{d_{\max}}{\varepsilon} \sim \varepsilon$).

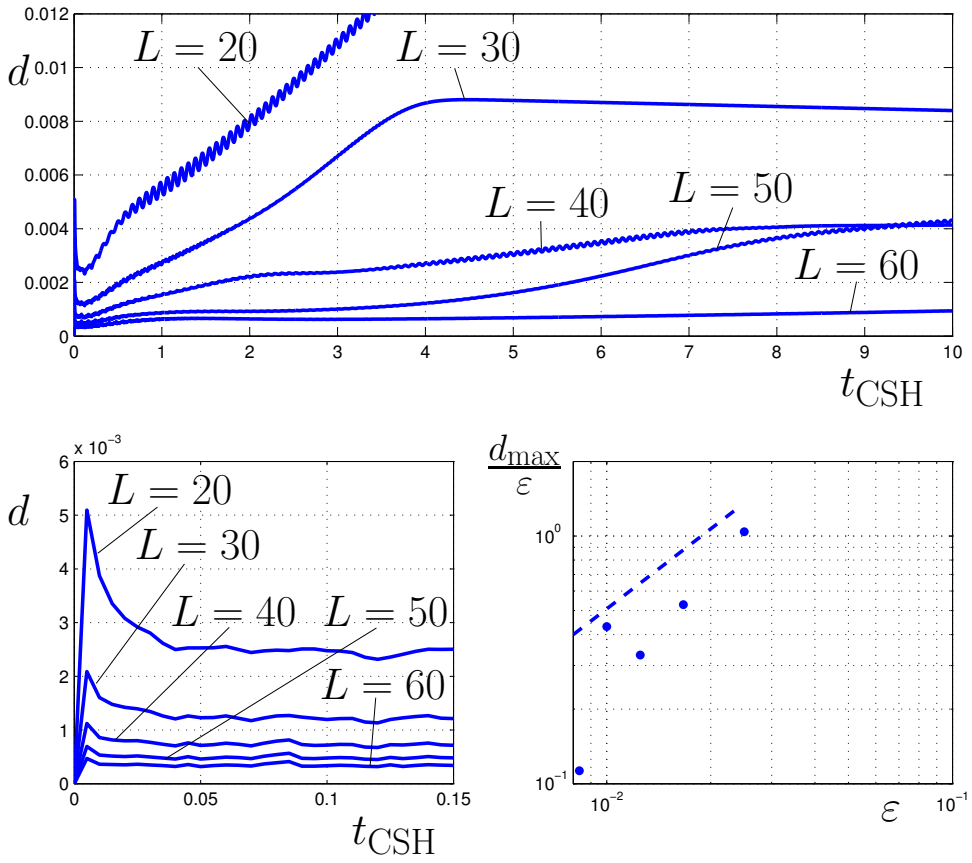

Figure 20: Top plot: Time evolution of the difference of the solution of the CSH and MB equations for $\sigma = 1$, $b = 1$, $\alpha = 0.5$, $\omega = 2$ and $L = 20, 30, 40, 50$ and 60. Bottom plot: short time detail of evolution of difference (left) and (right) the resulting maximum values of the difference versus ε (the dashed line corresponds to a decay $\frac{d_{\max}}{\varepsilon} \sim \varepsilon$).

5.3 Numerical integration of the MB equations

The Maxwell-Bloch equations (1)-(3) with periodic boundary conditions in a square domain of size L,

$$(E,P,N)(x+L,y,t)=(E,P,N)(x,y,t),\ (E,P,N)(x,y+L,t)=(E,P,N)(x,y,t),$$

are numerically integrated using a Fourier series representation in x and y, and a 4th order Runge-Kutta temporal scheme.

In order to do this, we expand the solutions in a double Fourier series of the form

$$(E,P,N)(x,y,t)=\sum_{k,j}(e_{k,j}(t),p_{k,j}(t),n_{k,j}(t))e^{\mathrm{i}(2\pi/L)\mathbf{k}\cdot\mathbf{x}},$$

with $\mathbf{k}=(k,j)$ and $\mathbf{x}=(x,y)$, and

$$n_{k,j}=\overline{n}_{-k,-j},$$

because the population inversion $N(x,y,t)$ is a real valued field. The resulting equations for the Fourier components can be written as

$$\begin{aligned}
\frac{de_{k,j}}{dt}&=-(\sigma+\mathrm{i}(2\pi/L)^2(k^2+j^2))e_{k,j}+\sigma p_{k,j},\\
\frac{dp_{k,j}}{dt}&=-(1+\mathrm{i}\Omega)p_{k,j}+re_{k,j}-[NE]_{k,j},\\
\frac{dn_{k,j}}{dt}&=-bn_{k,j}+\frac{1}{2}[\bar{E}P+E\bar{P}]_{k,j}.
\end{aligned}$$

We have to use a sufficiently large number of Fourier modes in order to ensure that we are accurately solving the shortest spatial scales exhibited by the system, which are $\lambda\sim\sqrt{L}$. This implies that the number of Fourier modes, N_{F}, should be such that

$$N_{\mathrm{F}}\sim m_\lambda\sqrt{L},$$

where m_λ represents the number of modes used to describe the shortest scales, and $m_\lambda\sim 5-10$ typically. Therefore, the coefficient that comes from dispersion in the system above can be quite large and this can give rise to numerical instabilities in the usual explicit time integration schemes (see [25]).

This problem can be avoided if we integrate explicitly the linear diagonal terms to obtain

$$\frac{d}{dt}\begin{bmatrix} \mathrm{e}^{-c_{1k,j}t}u_{1k,j} \\ \mathrm{e}^{-c_{2k,j}t}u_{2k,j} \\ \mathrm{e}^{-c_{3k,j}t}u_{3k,j} \end{bmatrix} = \begin{bmatrix} \mathrm{e}^{-c_{1k,j}t}f_{1k,j}(u_{1k',j'}, u_{2k',j'}, u_{3k',j'}) \\ \mathrm{e}^{-c_{2k,j}t}f_{2k,j}(u_{1k',j'}, u_{2k',j'}, u_{3k',j'}) \\ \mathrm{e}^{-c_{3k,j}t}f_{3k,j}(u_{1k',j'}, u_{2k',j'}, u_{3k',j'}) \end{bmatrix},$$

where

$$\begin{aligned} u_{k,j} &= (u_1, u_2, u_3)_{k,j} = (e, p, n)_{k,j}, \\ c_{k,j} &= (c_1, c_2, c_3)_{k,j} = (-(\sigma + \mathrm{i}(2\pi/L)^2(k^2 + j^2)), -(1 + \mathrm{i}\Omega), -b), \\ f_{k,j} &= (f_1, f_2, f_3)_{k,j} = (\sigma u_{2k,j}, r u_{1k,j} - [NE]_{k,j}, \frac{1}{2}[\bar{E}P + E\bar{P}]_{k,j}), \end{aligned}$$

And then, we use a standard explicit fourth order Runge-Kutta method [25], which yields the following time marching scheme for a single time step of size Δt

$$u_{k,j}(t + \Delta t) = \mathrm{e}^{c_{k,j}\Delta t}u_{k,j}(t) + \tfrac{\Delta t}{6}[\mathrm{e}^{c_{k,j}\Delta t}K^1_{k,j} + 2\mathrm{e}^{c_{k,j}\Delta t/2}K^2_{k,j} + 2\mathrm{e}^{c_{k,j}\Delta t/2}K^3_{k,j} + K^4_{k,j}],$$

where the vectors $K^1_{k,j}$, $K^2_{k,j}$ and $K^3_{k,j}$ are given by

$$\begin{aligned} K^1_{k,j} &= f_{k,j}(u_{k'j'}(t)), \\ K^2_{k,j} &= f_{k,j}(\mathrm{e}^{c_{k'j'}\Delta t/2}u_{k'j'}(t) + \frac{\Delta t}{2}\mathrm{e}^{c_{k'j'}\Delta t/2}K^1_{k'j'}), \\ K^3_{k,j} &= f_{k,j}(\mathrm{e}^{c_{k'j'}\Delta t/2}u_{k'j'}(t) + \frac{\Delta t}{2}K^2_{k'j'}), \\ K^4_{k,j} &= f_{k,j}(\mathrm{e}^{c_{k'j'}\Delta t}u_{k'j'}(t) + \Delta t\mathrm{e}^{c_{k'j'}\Delta t/2}K^3_{k'j'}), \end{aligned}$$

and the products of the vectors by the exponentials of the form $\mathrm{e}^{c_{k,j}\Delta t}$ have to be performed component by component.

This integration procedure always handles the Fourier representation of the solution and it is transformed to physical space only during the computation of the nonlinear terms, which is performed in the following steps

$$u_{k,j} \xrightarrow{\text{to Phys.}} (E, P, N) \to (\sigma P, rE - NE, \frac{1}{2}[\bar{E}P + E\bar{P}]) \xrightarrow{\text{to Fou.}} f_{kj},$$

where the products of the amplitudes are computed in physical space and the so-

called 2/3 rule is used to remove the aliasing terms (see e.g. [26]).

This numerical procedure has been implemented in a FORTRAN code and the FFTW subroutines [27] are used to perform the Fourier transforms.

5.4 Numerical integration of the CSH equation

The numerical integration method for the CSH equation (17) in the square domain $[0,1]\times[0,1]$ with periodic boundary conditions,

$$\phi(x+1,y,t)=\phi(x,y,t),\ \phi(x,y+1,t)=\phi(x,y,t),$$

is completely similar to that described in the previous section for the MB. First the solution is expanded in Fourier series

$$\phi(x,y,t)=\sum_{k,j}\phi_{k,j}(t)\mathrm{e}^{\mathrm{i}(2\pi)\mathbf{k}\cdot\mathbf{x}},$$

with $\mathbf{k}=(k,j)$ and $\mathbf{x}=(x,y)$, and then the resulting system of ODE's for the Fourier modes

$$\frac{d\phi_{k,j}}{dt}=(\alpha-(2\pi)^2(k^2+j^2)(2\varepsilon\omega+\mathrm{i})-\varepsilon^2(2\pi)^4(k^2+j^2)^2)\phi_{k,j}-[\phi|\phi|^2]_{k,j}$$

is integrated with the same temporal marching scheme used for the MB. The linear terms are integrated explicitly with

$$\begin{aligned}&c_{k,j}=\alpha-(2\pi)^2(k^2+j^2)(2\varepsilon\omega+\mathrm{i})-\varepsilon^2(2\pi)^4(k^2+j^2)^2,\quad\text{and}\\&f_{k,j}=[\phi|\phi|^2]_{k,j},\end{aligned}$$

and the nonlinear terms are again computed in physical space

$$\phi_{k,j}\xrightarrow{\text{to Phys.}}\phi\to\phi|\phi|^2\xrightarrow{\text{to Fou.}}f_{k,j},$$

using the 2/3 rule for the aliasing terms (see e.g. [26]). In this case, the smallest spatial scale that we have to represent are the diffusive scales $\delta_{\text{diff}}\sim\sqrt{\varepsilon}\ll 1$ and thus the required number of Fourier modes goes as $N_{\text{F}}\sim m_\delta/\sqrt{\varepsilon}\gg 1$ with $m_\delta\sim 5-10$ typically.

This numerical procedure has been implemented in a FORTRAN code and the FFTW subroutines [27] are used to perform the Fourier transforms. This code is also used to integrate the CGL eq. (18) just by setting $\varepsilon = 0$.

Bibliography

[1] F.T. Arecchi and S. Boccaletti P. Ramazza. Pattern formation and competition in nonlinear optics. *Physics Reports*, 318:1–83, 1999.

[2] K. Staliunas and V.J. Sánchez-Morcillo. *Transverse Patterns in Nonlinear Optical Resonators*. Springer Tracts in Modern Physics. Springer-Verlag, 2003.

[3] M.C. Cross and P.C. Hohenberg. Pattern formation outside of equilibrium. *Rev. Mod. Phys.*, 65(3):851–1112, 1993.

[4] J. Lega, J.V. Moloney, and A.C. Newell. Swift-hohenberg equation for lasers. *Phys. Rev. Lett.*, 73(22):2978–2981, 1994.

[5] J. Lega, J.V. Moloney, and A.C. Newell. Universal description of laser dynamics near threshold. *Physica D*, 83:478–498, 1995.

[6] L.A. Lugiato, C. Oldano, and L.M. Narducci. Cooperative frequency locking and stationary spatial structutres in lasers. *J. Opt. Soc. Am. B*, 5(5):879–888, 1988.

[7] A.C. Newell and J.V. Moloney. *Nonlinear Optics*. Addison Wesley Publishing Co., 1992.

[8] L. M. Narducci and N. B. Abraham. *Laser Physics and Laser Instabilities*. World Scientific Publishing, 1988.

[9] Q. Feng, J.V. Moloney, and A.C. Newell. Amplitude instabilities of transverse travelling waves in lasers. *Phys. Rev. Lett.*, 71(11):1705–1708, 1993.

[10] I. Aranson and L. Tsimring. Domain walls in wave patterns. *Phys. Rev. Lett.*, 75(18):3273–3276, 1995.

[11] J.-F. Mercier and J.V. Moloney. Derivation of semiconductor laser mean-field and swift-hohenberg equations. *Phys. Rev. E*, 66:036221, 2002.

[12] A. Barsella, C. Lepers, M. Taki, and P. Glorieux. Swift-hohenberg model of a co2 laser with saturable absorber. *J. Opt. B: Quantum Semiclass. Opt.*, 1:64, 1999.

[13] C. Martel and J.M. Vega. Finite sise effects near the onset of the oscillatory instability. *Nonlinearity*, 9:1129–1171, 1996.

[14] J.M. Vega, E. Knobloch, and C. Martel. Nearly inviscid faraday waves in annular containers of moderately large aspect ratio. *Physica D*, 154:313–336, 2001.

[15] C.M. Bendr and S. A. Orszag. *Advanced Mathematical Methods for Scientists and Engineers*. McGraw-Hill, 1978.

[16] J. Kevorkian and J.D. Cole. *Perturbation Methods in Applied Mathematics*. Springer-Verlag, 1981.

[17] H. Chaté and P. Manneville. Phase diagram of the two dimensional complex ginzburg-landau equation. *Physica A*, 224:348–368, 1996.

[18] I.S. Aranson and L. Kramer. The world of the complex ginzburg-landau equation. *Rev. Mod. Phys.*, 74(1):99–143, 2002.

[19] D. Hochheiser, J.V. Moloney, and J. Lega. Controlling optical turbulence. *Phys. Rev. A*, 55:R4011–R4014, 1997.

[20] I. Aranson, D. Hochheiser, and J.V. Moloney. Boundary-driven selection of patterns in large aspect ratio lasers. *Phys. Rev. A*, 55(4):3173–3176, 1997.

[21] S. Longhi and A. Geraci. Swift-hohenberg equation for optical parametric oscillators. *Phys. Rev. A*, 54:4581–4584, 1996.

[22] M. Santagiustina, E. Hernández-García, M. San-Miguel, A. J. Scroggie, and G.-L. Oppo. Polarisation patterns and vectorial defects in type ii optical parametric oscillators. *Phys. Rev. E*, 65:036610(1–14), 2002.

[23] K. Staliunas, G. Slekys, and C.O. Weiss. Nonlinear pattern formation in active optical systems: shocks, domains of tilted waves, and cross-roll patterns. *Phys. Rev. Lett.*, 79:2658–2661, 1997.

[24] P. S. Hagan. Spiral waves in reaction-diffusion equations. *SIAM J Appl. Math.*, 42(4):762–786, 1982.

[25] J.D. Lambert. *Numerical Methods for Ordinary Differential Systems: The Initial Value Problem*. John Wiley and Sons, 1995.

[26] C. Canuto, H.Y. Hussani, A. Quarteroni, and T.A. Zang. *Spectral Methods in Fluid Mechanics*. Springer Series in Computational Physics. Springer-Verlag, 1988.

[27] M. Frigo and S.G. Johnson. *FFTW*. available at `http://www.fftw.org` , 2004.